A&A 403, 313–322 (2003)
DOI: 10.1051/0004-6361:20030289

Astronomy & Astrophysics

The dust activity of comet C/1995 O1 (Hale-Bopp) between 3 AU and 13 AU from the Sun⋆

M. Weiler[1], H. Rauer[1], J. Knollenberg[1], L. Jorda[2], and J. Helbert[1]

[1] Institute of Space Sensor Technology and Planetary Exploration, DLR, Rutherfordstrasse 2, 12489 Berlin, Germany
[2] Laboratoire d'Astrophysique de Marseille, Site Pereisc, 13376 Marseille Cedex 12, France

Received 27 November 2002 / Accepted 20 February 2003

Abstract. The active comet C/1995 O1 (Hale-Bopp) was target of an optical long-term monitoring program carried out at the European Southern Observatory (ESO) (Rauer et al. 1997, 2003). Longslit spectra and images were obtained at heliocentric distances from 4.6 AU to 2.9 AU preperihelion and 2.8 AU to 12.8 AU postperihelion. Based on these data, the dust activity of comet Hale-Bopp is analysed. The color of the dust coma and the Afρ parameter are determined. A model for the dust release from the cometary nucleus is presented and used to compute dust production rates. The dust to gas ratio is determined.

Key words. comets: general – comets: individual: Hale-Bopp

1. Introduction

The dust-to-gas abundance seems to vary from comet to comet. A statistical analysis of the amount of dust in comets from different origins (e.g. Kuiper-belt comets or Oort cloud comets) could reveal inhomogenities in the preplanetary cloud. To perform such analysis, it is necessary to determine the dust to gas ratio in the comae of a large number of comets. However, deriving the dust production rates of comets is difficult because only little is known about the physical and chemical properties of the dust grains.

To estimate the dust production of a comet from the quantity of scattered sunlight, a model is needed which has to take the scattering properties of the dust particles, their physical characteristics and velocities into account.

Comet C/1995 O1 Hale-Bopp was an extraordinary bright and active comet, thus being an ideal object for long-term observations to collect data over a wide range of heliocentric distances. Observations of comet Hale-Bopp over a time of five years can be used to analyse the dust activity and its variation with changing heliocentric distances.

2. Observations and basic data reduction

Comet C/1995 O1 Hale-Bopp was observed at optical wavelengths between April 1996 and January 2001 at the European Southern Observatory (ESO), Chile. Medium-resolution spectra and images were obtained during this long-term observation campaign, covering a range of heliocentric distances, $r_{\rm h}$, from 4.6 to 2.9 AU preperihelion and 2.8 to 12.8 AU postperihelion (see Table 1, details of the long-term observation program are described by Rauer et al. 2003).

Standard data reduction routines were applied to the spectra, including bias subtraction, flatfielding, wavelengths calibration, sky background subtraction and extinction correction. At large heliocentric distances, the sky background was determined from the edges of the long-slit spectra since the coma did not fill the entire slit length. At smaller distances, separate spectra of the sky were used for background determination. They were obtained close in time to the comet observations with a spatial offset up to 30′, but at the same elevation as the comet. The extinction corrections were performed using ESO standard extinction curves. Absolute flux calibration was performed using standard stars (Rauer et al. 2003). In order to separate the contributions of gaseous cometary emissions and scattered light by dust particles, a solar catalogue spectrum (Kurucz et al. 1984) was matched to the cometary spectra by convolution with a Gaussian profile and a polynomial fit. The fitted solar spectrum can be subtracted from the cometary spectrum to obtain the gaseous emissions.

In this work, the fitted solar spectra were treated as approximation of the continuum flux scattered by the cometary dust and used to analyse the dust activity at $r_{\rm h} < 6$ AU. Beyond 6 AU, the measured spectra were used directly, because no gas emission lines were present in the wavelengths interval used in this study. The wavelengths interval was limited to the range from 4100 Å to 6100 Å which is covered by most spectra of our data set. Stellar spectra from background stars were removed from longslit spectra by interpolation along the spatial direction. The photometric uncertainty of spectra is estimated to be ∼10%. However, additional uncertainties arise in the calibration of the cometary spectra, e.g. due to the separation of the continuum flux and the gas emission features. We estimate the total uncertainty to about 20–30%.

Send offprint requests to: M. Weiler,
e-mail: michael.weiler@dlr.de

⋆ Based on observations collected at the European Southern Observatory, Chile.

Table 1. Observations of Comet Hale-Bopp. n: number of comet spectra per night, r_h and Δ: heliocentric and geocentric distances, β: phase angle, $\Delta\psi$: spatial scale per pixel, $\Delta\lambda$: wavelength scale per pixel, x: slit width. Negative r_h indicates observations before perihelion on April 1, 1997.

Date	n	r_h [AU]	Δ [AU]	β [°]	Telescope	Instrument	$\Delta\psi$ [″/pix.]	$\Delta\lambda$ [Å/pix.]	$\times$ [″]
1996.04.25/26	1	−4.60	4.29	12.4	Danish 1.5 m	DFOSC	0.39	3.02	2.0
1996.04.26/27	5†	−4.59	4.27	12.4	Danish 1.5 m	DFOSC	0.39	3.02	2.0
1996.06.24/25	3	−3.98	2.99	3.9	Danish 1.5 m	DFOSC	0.39	3.03	2.0
1996.08.19/20*	2	−3.38	2.77	15.2	Danish 1.5 m	DFOSC	0.39	3.02	2.5
1996.08.18/19	2	−3.38	2.76	15.1	Danish 1.5 m	DFOSC	0.39	3.02	1.0
1996.08.23/24	2	−3.33	2.78	16.1	Danish 1.5 m	DFOSC	0.39	3.02	2.5
1996.10.02/03	1	−2.86	2.99	19.5	Danish 1.5 m	DFOSC	0.39	3.03	2.5
1996.10.03/04	1	−2.85	3.00	19.5	Danish 1.5 m	DFOSC	0.39	3.03	2.5
1997.09.20/21**	0	2.78	3.07	18.9	ESO 2.2 m	EFOSC2	0.16	1.95	2.0
1997.09.29/30*	2	2.89	3.10	18.8	ESO 2.2 m	EFOSC2	0.16	1.95	1.5
1997.09.30/10.1.	2	2.90	3.11	18.8	ESO 2.2 m	EFOSC2	0.16	1.95	1.5
1997.11.23/24*	4†	3.51	3.39	16.2	ESO 1.5 m	B&C	0.82	1.89	2.4
1997.12.06/07	4†	3.66	3.50	15.6	Danish 1.5 m	DFOSC	0.39	3.05	1.5
1997.12.07/08*	4	3.67	3.51	15.6	Danish 1.5 m	DFOSC	0.39	3.05	1.5
1997.12.19/20	5†	3.78	3.62	15.0	ESO 1.5 m	B&C	0.82	1.89	2.4
1998.01.20/21	3	4.14	4.00	13.8	ESO 1.5 m	B&C	0.82	1.88	2.4
1998.01.21/22	4	4.15	4.02	13.7	Danish 1.5 m	DFOSC	0.39	3.04	2.0
1998.01.22/23	3	4.16	4.03	13.7	Danish 1.5 m	DFOSC	0.39	3.04	2.0
1998.03.17/18	3	4.71	4.75	12.1	Danish 1.5 m	DFOSC	0.39	3.05	2.0
1998.03.21/22	5	4.75	4.81	12.0	ESO 1.5 m	B&C	0.82	1.88	2.4
1998.08.05/06	1	6.05	6.21	9.4	ESO 1.5 m	B&C	0.82	1.89	1.6
1998.11.23/24	3	7.01	7.07	8.0	ESO 3.6 m	EFOSC 2	0.16	0.97	2.0
1998.11.24/25	2†	7.02	7.08	8.0	ESO 3.6 m	EFOSC 2	0.16	0.97	2.0
1999.01.13/14	6†	7.44	7.50	7.5	ESO 3.6 m	EFOSC 2	0.16	1.94	2.0
1999.01.14/15	2	7.44	7.50	7.5	ESO 3.6 m	EFOSC 2	0.16	1.95	2.0
1999.03.13/14	2	7.92	7.38	7.2	ESO 3.6 m	EFOSC 2	0.16	1.95	2.0
1999.11.12/13	2	9.78	9.89	5.7	VLT UT1	FORS 1	0.20	5.33	2.0
2000.04.05/06***	0	10.81	10.84	5.3	VLT UT1	FORS 1	0.20	5.33	2.0
2000.09.28/29	5	12.01	12.04	4.8	VLT UT1	FORS 1	0.20	2.61	2.0
2000.09.29/30	3	12.02	12.06	4.8	VLT UT1	FORS 1	0.20	2.61	2.0
2001.01.20/21	5	12.75	12.95	4.3	VLT UT1	FORS 1	0.20	2.61	2.0
2001.01.25/26	5	12.78	12.97	4.3	VLT UT1	FORS 1	0.20	2.61	2.0

* Night not photometric, only used for reddening determination. ** No flux calibration, night not used.
*** Magellan cloud in background, night not used.
† Slit orientations along projected solar direction and perpendicular to it.

Due to scattered background light on the CCD at the Danish 1.5 m telescope, wavelengths shorter than approximately 4600 Å could not be used for analysis in this work in data taken at this telescope.

To allow a test of the results obtained from longslit-spectra and to search for spatial structures in the coma of comet Hale-Bopp, *B*- and *R*-filter images were used. The reduction includes bias-, flatfield and sky background correction. Images of standard stars according to Landolt (1992) were used for photometric calibration. The calibration was performed by using the standard extinction and color correction terms as provided by ESO. The accuracy of the photometric calibration could be estimated by calibrating images of different standard star fields with the same star used to calibrate the comet images. We estimate the uncertainty in the comet magnitudes to be ~5%. An overview on the reduced images is given in Table 2.

3. Reddening

As a measure of the wavelengths dependent scattering of solar light by dust particles, the reddening $\mathcal{R}$ is computed. It is defined as (Jewitt & Meech 1986):

$$\mathcal{R}(\lambda_1, \lambda_2) = (\mathrm{d}\tilde{\mathcal{R}}/\mathrm{d}\lambda)/\tilde{\mathcal{R}}_{\mathrm{mean}}. \quad (1)$$

If F_λ denotes the wavelengths dependent flux,

$\tilde{\mathcal{R}} = F_\lambda/F_\lambda(\mathrm{sun})$ and $\mathrm{d}\tilde{\mathcal{R}}/\mathrm{d}\lambda$ is the rate of change of $\tilde{\mathcal{R}}$ within the wavelengths interval $[\lambda_1,\lambda_2]$. $\tilde{\mathcal{R}}_{\mathrm{mean}}$ is the mean value of $\tilde{\mathcal{R}}$ over the wavelengths interval. The reddening is computed

Table 2. Overview of *B*- and *R*-filter images used here. r_h and Δ denote heliocentric and geocentric distances. The standard star used for calibration of the comet images is quoted. The calibrations were performed using the standard star from each field with color indices similar to the solar colors.

night	r_h [AU]	Δ [AU]	standard star
2000.09.28/29	12.01	12.04	SA98–682
2000.09.29/30	12.02	12.06	SA98–682
2001.01.20/21	12.75	12.95	SA95–105
2001.01.25/26	12.78	12.97	PG 1323–086 C

Table 3. Comparison of the reddening from spectra, *R*(spectra), on the wavelength interval [4400 Å, 7100 Å] and from *B* and *R* filter images, *R*(images). (* Result possibly affected by cirrus clouds during observation of spectrophotometric standard star).

night	r_h [AU]	*R*(spectra) [%/10^3 Å]	*R*(images) [%/10^3 Å]
2000.09.28/29	12.01	4.1 ± 0.2	4.4 ± 3.1
2000.09.29/30	12.02	5.1 ± 1.4	4.6 ± 2.9
2001.01.20/21	12.75	3.5 ± 0.8	5.2 ± 2.1
2001.01.25/26	12.78	$-0.1 \pm 1.4^*$	4.4 ± 3.0

for each position along the slit to obtain a reddening profile through the cometary coma.

A comparison of the reddening of spectra, given in [%/10^3 Å], and reddening values obtained from image photometry using broad-band filters, *B* and *R*, is possible by applying the relation given by Jockers (1999),

$$\frac{\mathcal{R}}{100} = \frac{10^{0.4(B-R)} - 1}{10^{0.4(B-R)} + 1} \frac{2000}{\lambda_R - \lambda_B}. \quad (2)$$

Here, $B = (B)_{\rm comet} - B_\odot$ and $R = (R)_{\rm comet} - R_\odot$ denote the difference between the cometary and solar magnitudes. λ_B and λ_R are the effective wavelengths of the *B*- and *R*-filter used. The solar magnitude used is $B_\odot = -26^{\rm mag}.10$ (Cox 2000), $(B-V)_\odot = 0^{\rm mag}.65$, $(V-R)_\odot = 0^{\rm mag}.36$ (Kidger et al. 1998).

As an example, the reflectivity $\tilde{\mathcal{R}}$ obtained from long-slit spectra on August 28/29, 2001 is shown in Fig. 1, normalized at 6000 Å. Two nearly linear sections can be seen. Hence straight lines are fitted to the reflectivity curves in the wavelengths intervalls from 4100 Å to 5400 Å (here called "blue") and 5400 Å to 6100 Å (here called "red") to compute $\mathcal{R}$.

Only slight variations in the reddening along the slit have been found. Fig. 2 shows the reddening profile for one night as example.

We determined the mean reddening averaged along the slit. At large heliocentric distances, the dust coma was smaller than the projected slit length. The projected nucleocentric radius covered was then limited to a signal to noise ratio larger than five times the background noise, which could be determined at the edges of the slit. When the coma filled the whole projected slit length at small heliocentric distances, the range of nucleocentric distances used was selected based on a sufficiently high signal-to-noise ratio.

In Fig. 3 the computed mean reddening values in the cometary coma are shown. All spectra of one night with the same slit orientation were averaged. Since the blue wavelengths range was not available for observations with the Danish 1.5 m telescope due to background light on the CCD, no normalized reflectivity gradients could be derived in the wavelengths interval [4100 Å, 5400 Å] preperihelion.

The reddening obtained from *B*- and *R*-filter images, with effective wavelengths at 4400 Å and 7100 Å, are compared to the reddening obtained from spectra in Table 3 for data at large heliocentric distances. The results are in fairly good agreement. No significant spatial variations in reddening have been seen in these images, confirming the result from longslit spectra.

Figure 3 shows no significant change in reddening with heliocentric distance up to nearly 13 AU. Previous publications (Jewitt & Meech 1986, 1988) on other comets also report no systematic trends in reddening of cometary comae up to heliocentric distances of 6 AU.

The dust color depends on the grain size, the grain shape and the optical constants of the material forming the dust particles. Since one would not expect the shape and optical constants of cometary dust to change dramatically with heliocentric distance, the size distribution of the dust particles should be the major influence on the measured reddening. Although the maximum grain radius for particles that could be lifted from the nucleus surface is expected to decrease below 10 μm (see Sect. 5) in the range of heliocentric distances covered by our observations, the size of dust grains dominating the optical light scattering is about 0.5 μm (Williams et al. 1997; Jones & Gehrz 2000) and thus much smaller than the maximum grain size derived with the model described in Sect. 5. Hence, the optical light scattering is not expected to be affected by the variation of the dust size distribution within the considered range of heliocentric distances. Therefore, the dust reddening derived from optical observations is expected to be constant on a wide range of heliocentric distances, as confirmed by our observations.

4. Afρ parameter

The parameter Afρ was introduced by A'Hearn et al. (1984) as

$$\mathrm{Af}\rho = \frac{(2r_h\Delta)^2}{\rho} \frac{F_{\rm comet}}{F_\odot}. \quad (3)$$

Here, ρ denotes the projected radius of a diaphragm at the distance of the comet used in photometric observations and $F_{\rm comet}$ is the cometary flux measured in this diaphragm. Δ and r_h are the geocentric distance, e.g. in [cm], and heliocentric distance [AU], respectively. $F_\odot$ is the solar flux at $r_h = 1$ AU.

Afρ was calculated from *B*- and *R*-filter images for the nights listed in Table 2. All values were obtained using $\rho = 2 \times 10^5$ km. $F_\odot$ was taken from Cox (2000).

To obtain the quantity Afρ from long-slit spectra instead of aperture photometry, the expected flux through a spherical diaphragm centred on the nucleus with radius ρ is computed from the radial intensity profile along the slit. In order to do so, it has to be assumed that the cometary coma is rotationally symmetric. This method is, therefore, more sensitive to coma

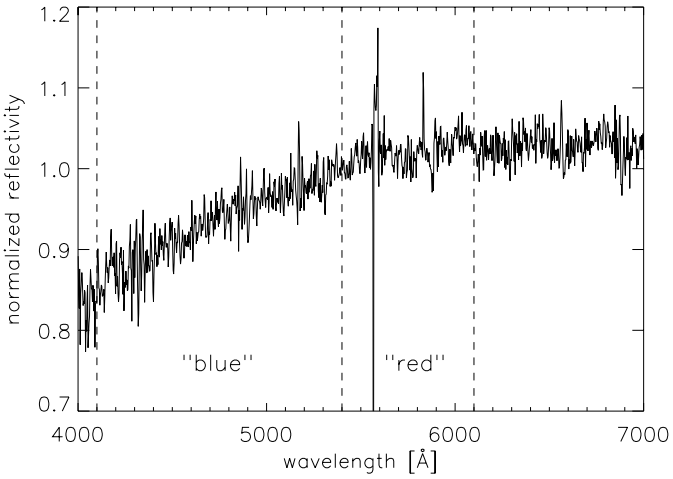

Fig. 1. Reflectivity, $\tilde{\mathcal{R}}$, of the coma of comet Hale-Bopp on January 20/21, 2001, averaged over 4600 km projected nucleocentric distance both sides of the nucleus and normalized at a wavelength of 6000 Å. The signature at approximately 5600 Å is a remnant of a night sky emission line. The "blue" and "red" intervals as described in the text are marked.

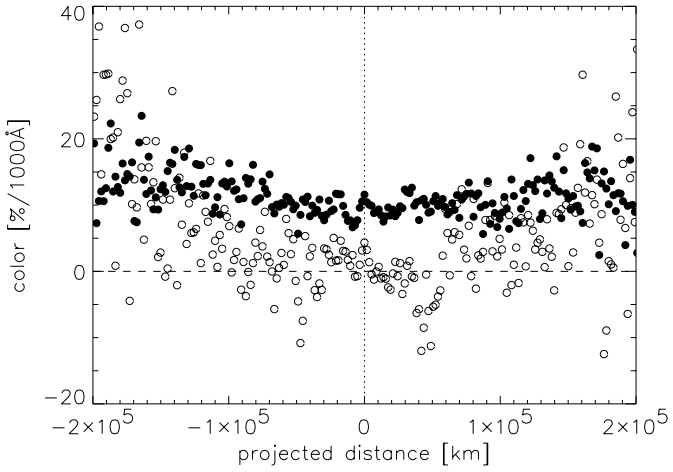

Fig. 2. Spatial reddening profile for August 28/29, 2000. Filled symbols show the reddening on the "blue" interval (4100 Å to 5400 Å), open symbols on the "red" interval (5400 Å to 6100 Å) along the slit versus projected distance from the nucleus. Negative distances denote the sunward side, positive distances the tailward side of the nucleus.

asymmetries than large aperture photometry. To estimate the effects of coma asymmetries, the expected flux is calculated using radial profiles along the sunward and tailward side of the cometary nucleus independently. The mean values of Afρ are determined by averaging Afρ derived from each side of the nucleus and from all spectra of one night, obtained with the same slit orientation. Afρ from radial intensity profiles show a weak dependency on the ρ used. For $\rho > 1.5 \times 10^5$ km, the variation was found to be less then approx. 20%. $F_\odot(\lambda)$ was taken from Kurucz et al. (1984).

The computed Afρ-parameters from *R*-filter images and long-slit spectra are shown in Fig. 4. For comparison, Afρ values from other publications are included. The bars connect the individual Afρ values computed using profiles from both

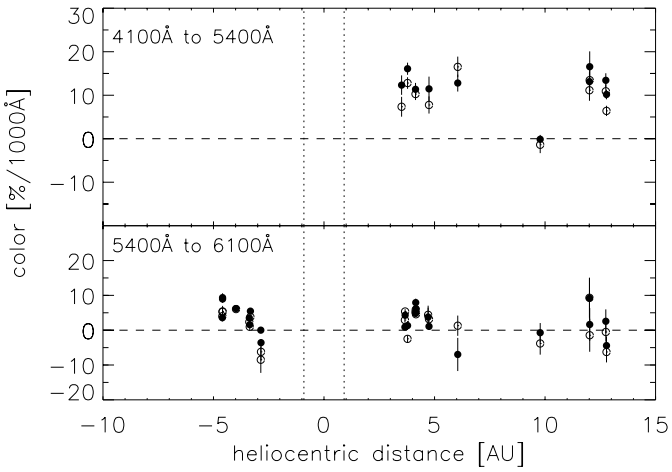

Fig. 3. Mean reddening in the coma of comet Hale-Bopp, for the "blue" wavelength interval (top panel) and the "red" interval (lower panel). Filled and open symbols mark data derived from the sunward and tailward side of the coma.

sides of the nucleus and are thus an indicator for the coma asymmetry.

The Afρ parameters obtained are in good agreement with previous publications and significantly extend the observed heliocentric distance range for comet Hale-Bopp.

5. Model for dust release

Assuming a spherical nucleus and isotropic emission of dust, the dust number and mass production rates, Q_N and Q_M, are related to the parameter Afρ by (Jorda 1995):

$$Q_N = \frac{\mathrm{Af}\rho}{2\pi^2 A_\mathrm{B}(\lambda) D(\beta)} \left[\int_{a_1}^{a_2} \frac{f(a) a^2}{v(a)} \,\mathrm{d}a \right]^{-1} \quad (4)$$

and

$$Q_M = Q_N \frac{4\pi}{3} \int_{a_1}^{a_2} \rho_\mathrm{dust}(a)\, a^3 f(a) \,\mathrm{d}a. \quad (5)$$

Here, a denotes the radius of the dust particles, A_B their Bond-albedo, $\rho_\mathrm{dust}(a)$ the size-dependent density of dust particles, $f(a)$ is the normalized size frequency distribution of dust particles, $v(a)$ is the size-dependent dust velocity with respect to the comet nucleus and $D(\beta)$ denotes the phase function. a_1 and a_2 are the minimum and maximum dust grain radii.

Unfortunately, only little is known about cometary dust. Therefore, a number of plausible assumptions have to be made in order to estimate the dust production rates.

In this work, the phase function $D(\beta)$ from Divine (1981) has been used:

$$D(\beta) = 0.634 - 0.678579(\pi - \beta) \quad (6)$$

for $\beta > 137°$, and

$$D(\beta) = 0.316908 - 0.340050(\pi - \beta) + 0.121087(\pi - \beta)^2 - 0.012235(\pi - \beta)^3 \quad (7)$$

for $\beta < 137°$.

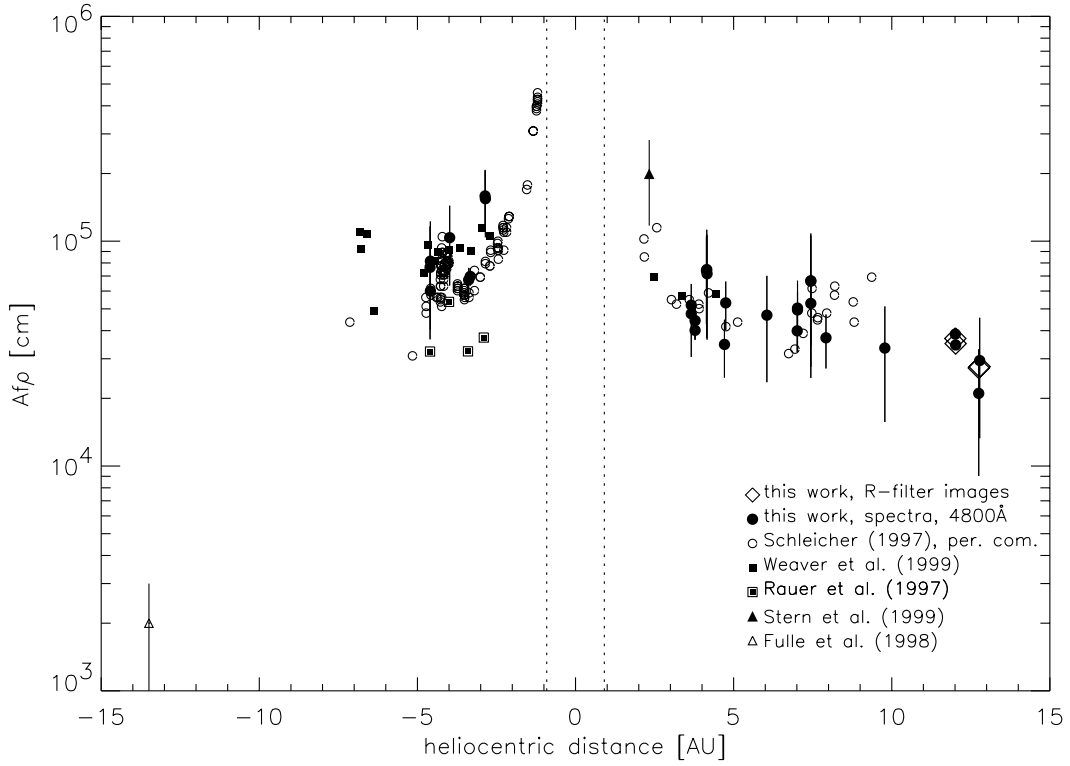

Fig. 4. Afρ from this work (from *R*-filter images and long slit spectra) and some previous publications. No corrections concerning the phase angle were applied on any of the shown data. Values from Schleicher are from observations made at Perth Observatory by Peter Birch, reductions by David Schleicher and supplied by personal communication. The dotted lines indicate the perihelion distance.

In the range of phase angles β of our observations of comet Hale-Bopp, this phase function corresponds to a correction to zero phase angle of approximately 0.02 mag per degree. This is a low value compared to other assumptions, e.g. 0.035 mag per degree by Weaver et al. (1997). Corrections with 0.02 and 0.035 magnitudes per degree result in differences of 6% up to 31% for the fluxes corrected to zero phase angle.

A Bond-albedo A_B of 0.3 is assumed. This value is higher than the often assumed value of $A_B = 0.2$ and is based on values determined from optical and infrared observations (Mason et al. 2001; Grün et al. 2001) of comet Hale-Bopp. From these observations, higher albedos for comet Hale-Bopp than for most other comets are deduced, which is assumed to be caused by unusually small dust particles in the coma of comet Hale-Bopp (Williams et al. 1997; Mason et al. 2001).

The functions and parameters $f(a)$, $\rho_{\rm dust}$ and $a_1 = 0.1$ μm from Newburn & Spinrad (1985) are used. The dust size distribution function is:

$$f(a) = \tilde{N}\left(1 - \frac{a_1}{a}\right)^M \left(\frac{a_1}{a}\right)^N \cdot \tag{8}$$

This distribution comprises a decrease in frequency for large particles according to a^{-N} and has a peak at $a_{\max} = a_1 \cdot \frac{M+N}{N}$. $\tilde{N}$ is a normalization factor, fulfilling the condition

$$\int_{a_1}^{a_2} f(a)\,{\rm d}a = 1. \tag{9}$$

Values of $N = 3.6$ and $M = 1.8$ were choosen, as derived from coma simulations (Fulle et al. 1998) and infrared observations (Williams et al. 1997) for comet Hale-Bopp.

The dust density is assumed by Newburn & Spinrad (1985) as

$$\rho_{\rm dust}(a) = \rho_0 - \rho_1\left(\frac{a}{a+\tilde{a}}\right)\cdot \tag{10}$$

With $\rho_0 = 3000\ \frac{\rm kg}{\rm m^3}$, $\rho_1 = 2200\frac{\rm kg}{\rm m^3}$ and $\tilde{a} = 2$ μm. This function $\rho_{\rm dust}(a)$ implies a higher density for small particles than for large dust grains and thus takes the structure of interplanetary dust particles into account. Dust particles collected in the Earth atmosphere and thought to originate from comets show a fluffy structure with a bulk density below the typical densities of minerals (Le Sergeant D'Hendecourt & Lamy 1980).

In order to determine $v(a)$ and a_2, a gasdynamical model for the gas stream caused by sublimation of the comet nucleus is used. The dust particles are then treated as test particles affected by this gas stream.

The gas flow is determined by the Euler-equations. They are solved in spherical coordinates as given by Körösmezey & Gombosi (1990), neglecting the influence of the dust on the gas flow:

$$\frac{\partial}{\partial t}\boldsymbol{w} + \frac{1}{\boldsymbol{r}^2}\frac{\partial \boldsymbol{r}^2 \boldsymbol{G}}{\partial \boldsymbol{r}} = \boldsymbol{S}, \tag{11}$$

where

$$\boldsymbol{w} = \begin{pmatrix} \rho_{\rm gas} \\ \rho_{\rm gas} u_{\rm gas} \\ \rho_{\rm gas}\, e \end{pmatrix}, \tag{12}$$

$$\boldsymbol{G} = \begin{pmatrix} \rho_{\rm gas} u_{\rm gas} \\ \rho_{\rm gas} u_{\rm gas}^2 + p_{\rm gas} \\ u_{\rm gas}(\rho_{\rm gas}\, e + p_{\rm gas}) \end{pmatrix}, \tag{13}$$

$$\boldsymbol{S} = \begin{pmatrix} 0 \\ \frac{2}{r} p_{\rm gas} \\ 0 \end{pmatrix}. \tag{14}$$

Here, $u_{\rm gas}$, $\rho_{\rm gas}$ and $p_{\rm gas}$ denote the gas velocity, density and pressure, respectively, and e is the total specific energy of the gas.

We neglect the influence of the dust on the gas flow in our model, although in case of large dust mass loading of the gas stream this effect can be significant. However, in case of comet Hale-Bopp at the heliocentric distances of our observations, the observed gas velocity in the coma, $v_{\rm gas}$, fitted by $v_{\rm gas} = 1.12 \cdot r_{\rm h}^{-0.41}$ km s^{-1} (Biver et al. 1999), can be well approximated by the terminal gas velocity corresponding to isentropic expansion of a mixture of water and carbon monoxide from a gas reservoir at the sublimation temperature T_0 (Landau & Lifschitz 1993). If the influence of dust on the gas flow would be significant, one would expect a higher gas velocity in the coma than derived from a reservoir outflow model since the dust would transfer heat to the gas and thus lead to a higher gas velocity. This is not observed and we, therefore, consider the influence of the dust on the gas flow to be negligible at the distance range considered here.

We now discuss the inner boundary conditions. The inner boundary conditions, $u_{\rm gas}$, $\rho_{\rm gas}$ and $p_{\rm gas}$ at the surface of the comet nucleus, were determined from a reservoir outflow model in conjunction with a fit to the observed gas production rates as described below.

The velocity $u_{\rm gas}$ at the surface is computed assuming the gas to flow with Mach number $M = 1$ from a nucleus surface with temperature T_0. This leads to (Knollenberg 1994)

$$u_{\rm gas}^{\rm surface} = \sqrt{\gamma k_{\rm B} \frac{T}{m}} \tag{15}$$

and

$$T = \frac{T_0}{1 + \frac{1}{2}(\gamma - 1)}. \tag{16}$$

For the molecular mass, m, and the adiabatic coefficient of the sublimated gas, γ, averaged values derived from an interpolation/extrapolation of measured H_2O and CO production rates are used. The surface temperature T_0 was calculated from an energy balance on the nucleus surface, including irradiation, thermal emission and sublimation. Heat conduction into the interior of the nucleus is neglected. This leads to (Kührt 1999):

$$\frac{F_\odot (1 - A^{(N)})}{r_{\rm h}^2} \cos(\beta) = \epsilon \sigma T_0^4 + H\, z_{\rm gas}. \tag{17}$$

Here, $A^{(N)}$ is the nucleus albedo, assumed to be equal to 0.04, and β denotes the solar zenith angle. ϵ is the surface emissivity, assumed to be 1. $z_{\rm gas}$ is the gas sublimation rate per surface area and H the sublimation heat, assumed to be $2.66 \times 10^6 \frac{\rm J}{\rm kg}$ (Kührt 1999) for water. In case of a CO dominated coma, CO is assumed to obtain the temperature of the surrounding water ice, for example by diffusing to the nucleus surface from a subsurface sublimation front.

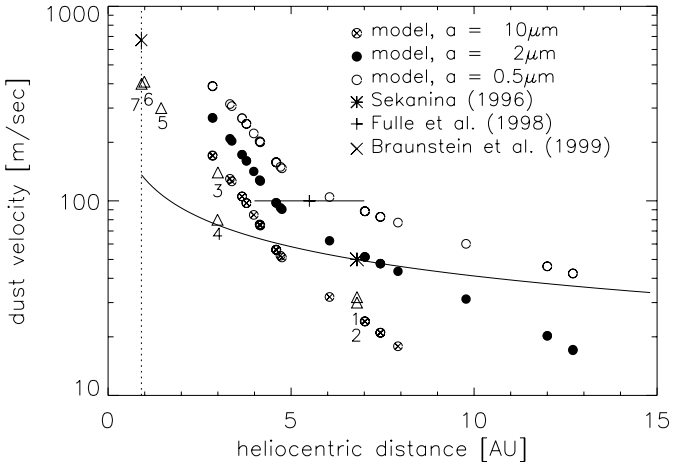

Fig. 5. Size dependent nucleocentric terminal dust velocities. The dust velocities calculated for grain radii $a = 10$ μm, 2 μm and 0.5 μm, are shown. Dust ejection velocities derived from observations are shown for comparison. The dust velocity from Fulle et al. (1998) is derived from coma modeling for a particle radius of 10 μm. The values from Braunstein et al. (1999) and Sekanina (1996) are dust ejection velocities estimated from movements of coma structures. The triangles give projected dust velocities (thus lower limits) from different publications as derived from observations of coma features: 1: Kidger et al. (1996), 2: Sekanina (1996), 3: Tozzi et al. (1999), 4: McCarthy et al. (1999), 5: Lecacheux et al. (1997), 6: Warell et al. (1999),7: Lisse et al. (1999). The line indicates a dependency according to $v_{\rm dust} \sim r_{\rm h}^{-0.5}$.

For the sublimation rate $z_{\rm gas}$ an approach according to Fanale & Salvail (1984) is used:

$$z_{\rm gas} = {\rm C}_1\, e^{-\frac{{\rm C}_2}{T_0}} \left(\sqrt{2\pi k_{\rm B} \frac{T_0}{m}} \right)^{-1}. \tag{18}$$

Equations (17) and (18) were solved using $C_1 = 3,56 \times 10^{12}$ Pa and $C_2 = 6141$ K for water ice (Fanale & Salvail 1984). With T_0 from Eqs. (17) and (18) and using $\beta = 45°$, $u_{\rm gas}^{\rm surface}$ can be computed.

In most cases, measurements of H_2O and CO production rates of comet Hale-Bopp do not exist for the exact heliocentric distances of our observations. They, therefore, had to be interpolated and extrapolated to our observing dates from the various existing production rate determinations. Equations (17) and (18) were used to compute the water production rates versus heliocentric distance. Then, $4\pi {R_N}^2 \cdot z_{\rm gas}(r_{\rm h})$ was fitted to the observed water and OH production rates given by Weaver et al. (1999), Weaver et al. (1999), Stern et al. (1999) and DiSanti et al. (1999) by a scaling factor, $\mathcal{W}$. For this, the nucleus radius, R_N, is needed. Values of R_N range from 22 km (Altenhoff et al. 1999) to 35 km (Sekanina 1999). Here, R_N is assumed to be 30 km. The fitted solution agrees well with the observed data and was used to obtain the water production rate at the heliocentric distances of our observations. The CO production rates were determined by fitting a power law to the measured production rates as given by Biver et al. (1999).

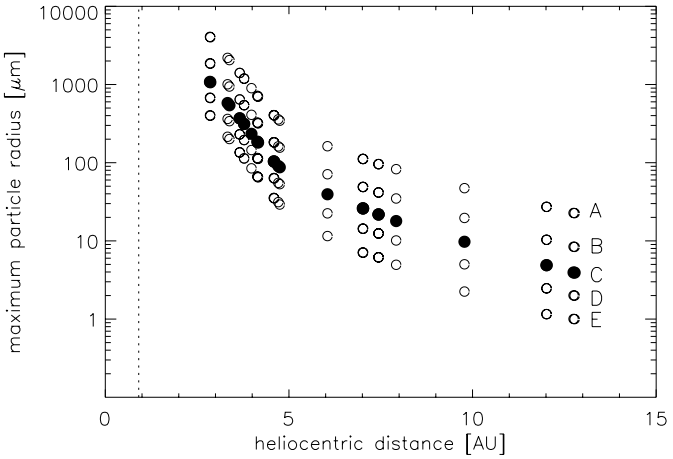

Fig. 6. Maximum dust grain radii $a_{\max}$ that can be lifted from the nucleus surface of comet Hale-Bopp versus heliocentric distance. $a_{\max}$ is shown for different model parameters (see text): A: R_N = 30 km, f = 5%, B: R_N = 25 km, f = 19 %, C: R_N = 30 km, f = 19%, D: R_N = 35 km, f = 19%, E: R_N = 30 km, f = 50%. The filled symbols mark $a_{\max}$ as used for the determination of the dust production rates.

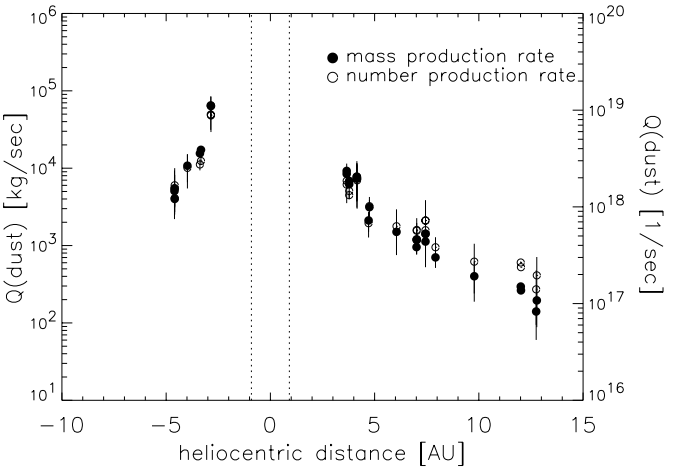

Fig. 7. Dust production rates, determined with the model described in Sect. 5. Filled symbols show mass production rates (left scale), empty symbols production rates by number (right scale).

The gas density at the nucleus surface, $\rho_{\rm gas}^{\rm surface}$, was determined by distributing the gas production rate determined from the fit to the observed values over an active nucleus surface area:

$$\rho_{\rm gas}^{\rm surface} = \mathcal{W} \cdot Q_{\rm gas} \cdot m \, (4\pi {R_N}^2 \cdot f \cdot u_{\rm gas}^{\rm surface})^{-1}. \quad (19)$$

The active surface fraction of the nucleus, f, takes the existence of jets into account. The gas and dust activity of the comet nucleus is assumed to originate from this active surface fraction. Unfortunately, only crude estimates for f can be made. We choose the following approach.

A more sophisticated model for water production of comet Hale-Bopp (Kührt 1999) than applied in this work deduces a nuclear radius of 13 km for a pure water ice sphere necessary to produce the observed quantity of water released by comet Hale-Bopp. This leads, in combination with R_N, to an active surface fraction of approximately 19%, which is assumed here as our nominal value of f.

Finally, $p_{\rm gas}^{\rm surface}$ follows from the ideal gas law:

$$p_{\rm gas}^{\rm surface} = \rho_{\rm gas}^{\rm surface} k_{\rm B} T \quad (20)$$

The velocity of a dust particle in the gas flow is determined by solving the equation of motion as given by Probstein (1969):

$$\frac{4}{3}\pi\rho_{\rm dust}(a)a^3\frac{{\rm d}v(a)}{{\rm d}t} = \frac{1}{2}C_D\rho_{\rm gas}\pi a^2(u_{\rm gas} - v(a))^2 - {\rm G}\,\frac{16}{9}\pi^2\rho_{\rm dust}(a)a^3 \cdot \rho_N {R_N}^3 \frac{1}{r^2}. \quad (21)$$

In Eq. (21), G denotes Newtons gravitational constant. The drag coefficient $C_{\rm D}$ is given by Probstein (1969) for free molecular dust-gas interaction. ρ_N denotes the nucleus density, assumed to be $10^3 \frac{\rm kg}{\rm m^3}$. The maximum dust particle radius lifted from the nucleus, a_2, can be obtained from Eq. (21) by setting the acceleration in the gas stream equal to the gravitational acceleration.

The Euler-Eq. (11) were solved using a Godunov-type scheme of second order (Harten et al. 1983). The equation of motion for dust particles was solved by using a Runge-Kutta scheme of fourth order. In Eq. (4), the velocity $v(a)$ computed at a nucleocentric distance of 10^3 km was used. The gas density decreases rapidly with increasing nucleocentric distance and, thus, the dust decouples within a few nuclear radii above the surface (Probstein 1969). Therefore, $v(a)$ calculated at 10^3 km from the nucleus is a good aproximation of the terminal velocity of a dust particle.

The dust velocities for some dust grain radii obtained using this model are shown in Fig. 5, together with dust velocities from other publications. The dust velocity from Fulle et al. (1998) was derived from coma simulations for particles of 10 μm radius. The dust velocities from Braunstein et al. (1999) and Sekanina (1996) were estimated from observations of moving coma structures. Projected dust velocities as determined from observations of coma features are also given. These values were derived from both optical and infrared observations and do not refer to a particular dust grain size. Since the dominant contribution to the observed light scattered by dust comes from particles with sizes similar to the wavelength of the light, the observational projected dust velocities are lower limits for dust grains with radii of approximately 0.5 μm to a few microns. A good agreement between our model results and observational data over a wide range of heliocentric distances is found within the observational and modelling uncertainties.

The maximum radii of dust grains lifted from the nucleus calculated with different model parameters are shown as a function of heliocentric distance in Fig. 6. A strong influence of the assumed nucleus radius (in Fig. 6: 25 km, 30 km, 35 km, compare B, C, D) and the assumed active surface fraction (in Fig. 6: 5%, 19%, 50%, compare A, C, E) can be seen. An active surface fraction of 50% means the gas production to originate from the whole sunward hemisphere of the nucleus. 5% active fraction means a lower limit, for a nucleus with 30 km radius, just enough to explain the observed water production rates with our simple model using constant zenith angle.

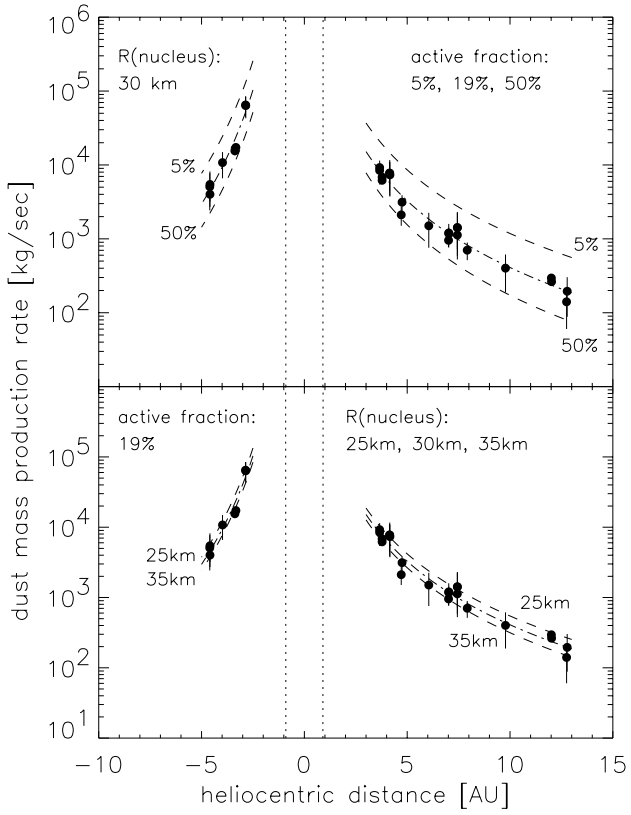

Fig. 8. Dust mass production rates for different model parameters. Upper panel: R_N = 30 km and active surface fractions f of 5%, 19% and 50% of the total surface. Lower panel: active surface fraction f = 19% and R_N of 25 km, 30 km and 35 km. The values for the preferred parameters (R_N = 30 km, f = 19%) are shown (dots) and power law fits to the dust production rates calculated with the different parameters are plotted.

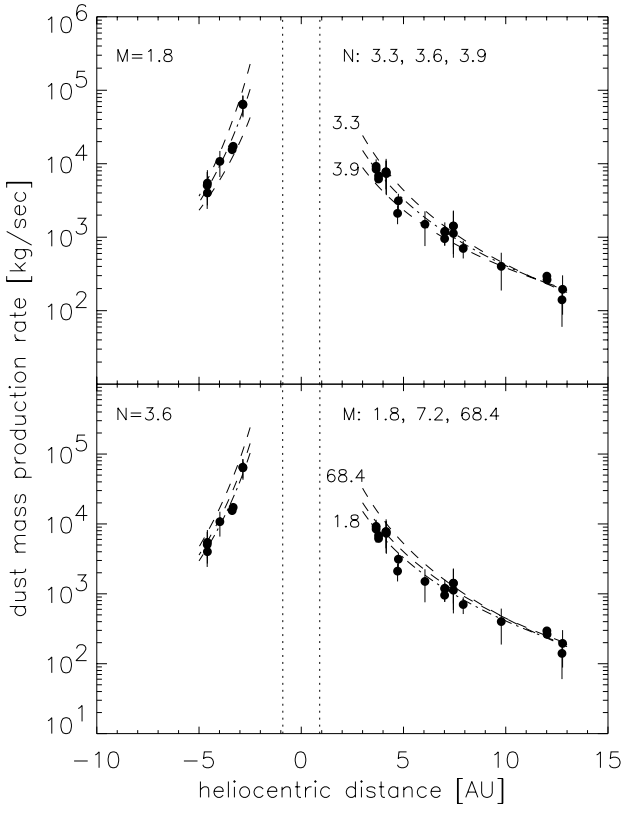

Fig. 9. Dust mass production rates for different model parameters. Upper panel: dust size distribution parameter M = 1.8 and N = 3.3, 3.6 and 3.9. Lower panel: N = 3.6 and M = 1.8, 7.2 and 68.4 The parameters N and M correspond to a peak in the dust size distribution at 0.15 μm, 0.3 μm and 2 μm. The values for the preferred parameters (M = 1.8, N = 3.6) are shown (dots) and power law fits to the dust production rates calculated with the different parameters are plotted.

6. Dust production rates

The dust production rates computed with the model described above are shown in Fig. 7.

In order to estimate the influence of the different parameters used in this model, Fig. 8 shows the variation of the dust mass production rates with changing active surface fraction f at constant nucleus radius (upper panel) and with changing nucleus radius at constant f (lower panel). A strong increase of the dust production rate with decreasing f can be seen. When reducing f, the observed gas production is concentrated on a smaller surface area, thus leading to a higher gas density at the nucleus surface. From this, a higher dust terminal velocity and a larger liftable dust size results. A higher dust velocity and larger values of a_2 lead to an increase of the dust production rate.

A larger nucleus radius leads to a decrease of the dust mass production rate due to the influence of gravitation and gas density at the nucleus surface on the dust velocity and a_2. Assuming a minimum nucleus radius of 13 km and varing R_N and f with $R_N \cdot f$ = const. (meaning constant active surface area) leads to a lower a_2 for a larger R_N due to gravity, but to a higher dust terminal velocity since the gas density decreases more slightly for a larger radius. Therefore, only a weak variation of the dust production rate of some percent results from a combined variation of R_N and f.

The influence of the dust size distribution parameters M and N on the dust mass production rates are shown in Fig. 9. Even deviations from the size distribution parameters being larger than the uncertainties derived for comet Hale-Bopp (N = 3.6 ± 0.1 (Fulle et al. 1998), peak at $a_{\max} \approx 0.15$ μm, $a_{\max}$ at 0.3–0.5 μm for other comets (Williams et al. 1997) have only moderate influence on the dust production rates, compared to the influence of the nucleus parameters (Fig. 8). A reduction of the parameter a_1 by a factor of 2 leads to a mean variation of the dust mass production rates of approximately 15%.

In Fig. 10, the Afρ to gas mass ratios and dust to gas mass ratios are shown. The gas mass production rates are the sum of the H_2O and CO production rates, since these two molecules are the most abundant in the coma. For comparison, dust to gas mass ratios from different literature sources are also shown. The dust to gas ratios according to Weaver et al. (1999) were computed using their dust production rates and gas production rates determined as described in Sect. 5.

An increase of the Afρ to gas ratio with increasing heliocentric distance can be seen, as reported before (Rauer et al. 1997). This trend stops at approximately 7 AU to 8 AU from the Sun.

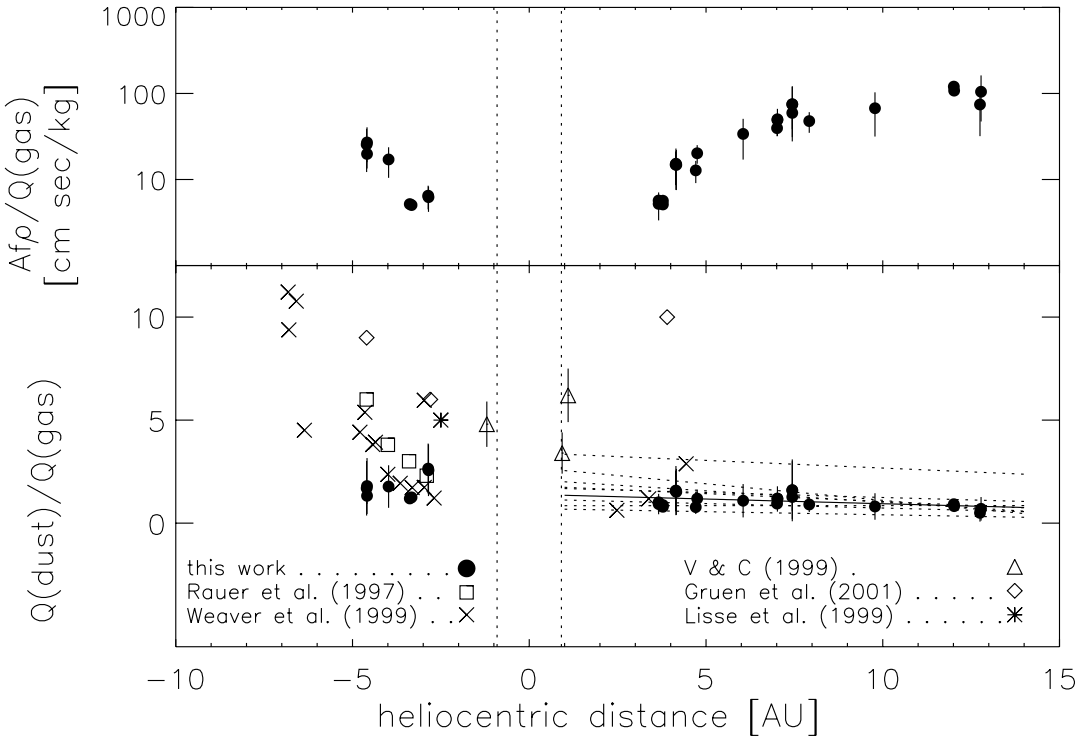

Fig. 10. Afρ to gas mass ratio (upper panel) and dust to gas mass production ratio (lower panel). In the lower panel, dust to gas mass ratios from other publications are shown. The values from Weaver et al. (1999) are calculated from the given dust production rates. Solid line postperihelion: linear fit to the dust to gas mass ratios from this work, computed with the prefered parameters. Dotted lines postperihelion: linear fits to the dust to gas mass ratios from this work, computed with model parameters as in Figs. 8 and 9. V & C (1999) stands for Vasundhara & Chakraborty (1999).

The dust to gas mass ratios obtained in this work are nearly constant with changing heliocentric distance. A linear least squares fit to the postperihelion mean values of $Q_M/Q_{\rm gas}$ over heliocentric distance leads to $(Q_M/Q_{\rm gas})^{\rm fit}(r_{\rm h}) = 1.40{-}0.05 \cdot r_{\rm h}$. The linear least squares fits to the dust to gas mass ratios obtained when using Q_M computed with the model parameters as shown in Figs. 8 and 9 are shown as dotted lines in Fig. 10. The highest dust to gas mass ratio follows from an active surface fraction of 5%, the lowest for an active surface fraction of 50%. A stronger dependency of light scattering on the phase angle (e.g. $0^{\rm mag}.035$ per degree) would lead to slightly higher dust to gas mass ratios and a steeper decrease with increasing heliocentric distance. Although the absolute values of the dust to gas mass ratios vary with changing model parameters, the slight decrease in the dust to gas mass ratio with increasing heliocentric distance can be seen for all parameters.

The trend in the dust to gas mass ratio differs from results published previously (e.g. Weaver et al. 1999; Rauer et al. 1997). This is caused by two effects. Firstly, the dust velocity is not assumed to follow a law of the form $v \sim r_{\rm h}^{-0.5}$, as done in the publications mentioned. Instead, the dust velocities used here are calculated by a reasonable physical model. A second influence is the increase of the maximum grain radius that can be lifted from the nucleus surface with decreasing heliocentric distance, thus allowing a larger mass of dust to be set free.

The presented approach to compute dust production rates leads to an approximately constant dust to gas mass ratio as a function of heliocentric distance. The increasing Afρ to gas ratio with increasing heliocentric distance up to ∼8 AU can be explained with the variation of dust velocity with changing heliocentric distance. Mechanisms proposed before, like albedo variations with varying heliocentric distance due to icy grains (A'Hearn et al. 1995; Rauer et al. 1997), are not necessary.

A rough estimate of the total dust production and the surface erosion during one perihelion passage can be made by integration of the dust production along the comets orbit. Assuming a dust to gas mass ratio of $(Q_M/Q_{\rm gas})^{\rm fit}(r_{\rm h}) = 1.40{-}0.05 \cdot r_{\rm h}$, calculating the water and CO production rates as described above and integrating from 20 AU pre-perihelion to 20 AU post-perihelion gives a total dust mass loss of about 1.1×10^8 kg. For a nucleus of 30 km radius and a density of $10^3 \frac{\rm kg}{\rm m^3}$, one obtains a mean surface erosion of nearly 1 m of dust and gas.

7. Summary

The continuum flux of scattered sunlight as measured by longslit spectroscopy was used to analyse the dust activity of comet C/1995 O1 Hale-Bopp at heliocentric distances between 2.9 AU and 12.8 AU.

The reddening of the dust was determined and no significant variation in dust reddening with changing heliocentric distance was found.

The Afρ parameters were derived from the spatial profiles of the longslit spectra and used to compute the dust production rates.

To compute the dust production rates, a spherical symmetric dust emission was assumed. The gas flow by sublimation of ices from the surface of the nucleus was computed using a gas-dynamical model. The dust particles were treated as spherical test particles within the gas flow. A size-dependent density and a size distribution of the dust particles were taken into account.

A dust to gas mass ratio of $(Q_M/Q_{\rm gas})^{\rm fit}(r_{\rm h}) = 1.40 - 0.05 \cdot r_{\rm h}$ for the preferred model parameters in this work was found, thus showing a very slight decrease with increasing heliocentric distance. This is a low value compared to other publications of dust-to-gas mass ratios for comet Hale-Bopp. However, due to the large influence of the nucleus size and the active surface fraction on the dust production rates, it is difficult to compare cometary dust production rates computed with simple models.

For example, if a Bond-albedo similar to other comets would be assumed for comet Hale-Bopp (e.g. 0.2), the dust to gas mass ratio would increase by a factor of 3/2. In most publications (Williams et al. 1997; Grün et al. 2001), the high value for the albedo is attributed to a large amount of small particles in comet Hale-Bopp's coma. This is consistend with a relatively low dust to gas mass ratio, nevertheless the comet appeared as one of the brightest comets for many years.

This work has shown that when deriving the coma dust flow from gasdynamical calculations, the variation of the dust to gas mass ratio with heliocentric distance is only weak. In particular, proper treatment of the gas and dust velocities with heliocentric distance is important to differentiate gas-dust dynamical effects from other influences on the observed parameters, such as icy grains or other sources of albedo variations.

References

A'Hearn, M. F., Millis, R. L., Schleicher, D. G., Osip, D. J., & Birch, P. V. 1995, Icarus, 118, 223

A'Hearn, M. F., Schleicher, D. G., Millis, R. L., Feldman, P. D., & Thompson, D. T. 1984, AJ, 89, 579

Altenhoff, W. J., Bieging, J. H., Butler, B., et al. 1999, A&A, 348, 1020

Biver, N., Bockelée-Morvan, D., Colom, P., et al. 1999, Earth Moon and Planets, 78, 5

Braunstein, M., Womack, M., Deglman, F., et al. 1999, Earth Moon and Planets, 78, 219

Cox, A. N., ed. 2000, Allen's Astrophysical Quantities, 4th ed. (Athlone Press)

DiSanti, M. A., Mumma, M. J., Dello Russo, N., et al. 1999, Nature, 399, 662

Divine, N. 1981, ESA-SP, 174

Fanale, F. P., & Salvail, J. R. 1984, Icarus, 60, 476

Fulle, M., Cremonese, G., & Böhm, C. 1998, AJ, 116, 1470

Grün, E., Hanner, M. S., Peschke, S. B., et al. 2001, A&A, 377, 1098

Harten, A., Lax, P. D., & van Leer, B. 1983, SIAM Rev., 25, 35

Jewitt, D., & Meech, K. J. 1986, AJ, 310, 937

Jewitt, D., & Meech, K. J. 1988, AJ, 96, 1723

Jockers, K. 1999, Earth Moon and Planets, 79, 221

Jones, T. J., & Gehrz, R. D. 2000, Icarus, 143, 338

Jorda, L. 1995, Ph.D. Thesis, Observatoire de Paris-Meudon

Kührt, E. 1999, Space Sci. Rev., 90, 75

Kidger, M. R., Serra-Ricart, M., Bellot Rubio, L. R., & Casas, R. 1996, ApJ, 461, L119

Kidger, M. R., Serra-Ricart, M., Licandro, J., et al. 1998, A&A, 329, 1152

Knollenberg, J. 1994, Ph.D. Thesis, Georg-August-Universität zu Göttingen

Körösmezey, A., & Gombosi, T. I. 1990, Icarus, 84, 118

Kurucz, R. L., Furenlid, I., Brault, J., & Testerman, L. 1984, Solar Flux Atlas from 296 to 1300 nm (Tech. rept. National Solar Observatory, Sunspot, New Mexico)

Landau, L. D., & Lifschitz, E. M. (ed.) 1993, Fluid Mechanics, 2nd ed. (Pergamon Press)

Landolt, A. U. 1992, AJ, 104

Le Sergeant D'Hendecourt, L. B., & Lamy, P. L. 1980, Icarus, 43, 350

Lecacheux, J., Jorda, L., Colas, F., et al. 1997, IAU Circ., 6560, 1

Lisse, C. M., Fernández, Y. R., A'Hearn, M. F., et al. 1999, Earth Moon and Planets, 78, 251

Mason, C. G., Gehrz, R. D., Jones, T. J., et al. 2001, AJ, 549, 635

McCarthy, D., Stolovy, S., Kern, S., et al. 1999, Earth Moon and Planets, 78, 243

Newburn, R. L., & Spinrad, H. 1985, AJ, 90, 2591

Probstein, R. F. 1969, in Problems of Hydrodynamics and Continuum Mechanics, 568

Rauer, H., Arpigny, C., Boehnhardt, H., et al. 1997, Science, 275, 1909

Rauer, H., Helbert, J., Arpigny, C., et al. 2003, A&A, 397, 1109

Sekanina, Z. 1996, A&A, 314, 957

Sekanina, Z. 1999, Earth Moon and Planets, 77, 147

Stern, S. A., Colwell, W. B., Festou, M. C., et al. 1999, AJ, 118, 1120

Tozzi, G. P., Mannucci, F., & Stanga, R. 1999, Earth Moon and Planets, 78, 279

Vasundhara, R., & Chakraborty, P. 1999, Icarus, 140, 221

Warell, J., Lagerkvist, C., & Lagerros, J. S. V. 1999, Earth Moon and Planets, 78, 197

Weaver, H. A., Feldman, P. D., A'Hearn, M. F., et al. 1997, Science, 275, 1900

Weaver, H. A., Feldman, P. D., A'Hearn, M. F., et al. 1999, Icarus, 141, 1

Williams, D. M., Mason, C. G., Gehrz, R. D., et al. 1997, ApJ, 489, L91